HHS Public Access

Author manuscript

Nat Nanotechnol. Author manuscript; available in PMC 2015 November 01.

Published in final edited form as:

Nat Nanotechnol. 2015 April ; 10(4): 370–379. doi:10.1038/nnano.2015.17.

Breaking the Depth Dependency of Phototherapy with Cerenkov Radiation and Low Radiance Responsive Nanophotosensitizers

Nalinikanth Kotagiri, **Gail P. Sudlow**, **Walter J. Akers**, and **Samuel Achilefu***

Department of Radiology, Washington University School of Medicine, St. Louis, MO 63110 USA

Abstract

The combination of light and photosensitizers for phototherapeutic interventions such as photodynamic therapy has transformed medicine and biology. However, the shallow penetration of light in tissues and the reliance on tissue oxygenation to generate cytotoxic radicals have limited the method to superficial or endoscope-accessible lesions. Here, we report a way to overcome these limitations by using Cerenkov radiation from radionuclides to activate an oxygen-independent nanophotosensitizer, titanium dioxide (TiO_2). We show that administration of transferrin-coated TiO_2 nanoparticles and clinical grade radionuclides in mice and co-localization in tumours resulted in either complete tumour remission or increased their median survival. Histological analysis of tumour sections showed selective destruction of cancerous cells and high numbers of tumour infiltrating lymphocytes, suggesting that both free radicals and the activation of the immune system mediated the destruction. Our results offer a way to harness low radiance-sensitive nanophotosensitizers to achieve depth-independent Cerenkov radiation-mediated therapy.

Breakthroughs in light-based diagnostic and therapeutic interventions have ushered new frontiers in biomedical research, as evidenced by recent advances in multiphoton microscopy, photoacoustic technology, targeted photoablation of tissue, photothermal therapies, photodynamic therapy (PDT), and image guided surgeries. Regardless of the method employed, light-based interventions suffer from the rapid attenuation of light in tissue, confining phototherapy to superficial structures[1] and requiring fibre light source to treat endoscope-accessible deep tissues[2].

We hypothesized that Cerenkov radiation (CR) could serve as a depth-independent light source for photo-induced therapy. CR occurs when charged particles such as positrons or electrons travel faster than the speed of light in a given medium, emitting predominantly

*Correspondence and requests for materials should be addressed to SA. achilefus@mir.wustl.edu.

Author contributions

N.K. and S.A. conceived and designed the experiments, analysed the data and wrote manuscript. N.K. performed most of the experiments. W.A. assisted in animal study design and analysis and contributed to editing of the final manuscript. G.S assisted in cell studies, animal handling, histological section preparation, and editing of final manuscript.

Additional information

Supplementary information accompanies this paper at www.nature.com/naturenanotechnology.

Competing financial interests

The authors declare no competing financial interests.

ultraviolet (UV) light that tails off to the visible spectrum (250–600 nm)[3,4]. Radionuclides such as radiolabelled 2′-deoxy-2′-(^{18}F)fluoro-D-glucose (FDG), which are widely used in positron emission tomography (PET), are an ideal sources for CR because of their high positron (β^+) emission decay and short half-life [5]. Recent technological advances in low light detection techniques have enabled the use of CR alone,[6,7] or its interaction with energy harvesting materials such as quantum dots[8,9] and porphyrins[10] (see Supplementary Discussion in Supplementary Information), as a light source for molecular imaging. Clinical application of CR imaging was recently demonstrated[11,12]. Despite these advances, CR remains a low intensity light source because of the low CR photon flux from the radiotracers, requiring significant signal amplification and prolonged data acquisition time, limiting the number of activatable materials.

TiO_2 nanoparticles are excellent regenerative photocatalysts that absorb UV light (λ= 275–390 nm) with high efficiency to generate cytotoxic hydroxyl and superoxide radicals[13]. The hydroxyl radicals are produced through electron-hole transfer to chemisorbed H_2O in an oxygen-independent process, whereas superoxide radical generation requires aerobic conditions for electron transfer to molecular oxygen (Fig. 1a)[14,15]. Because of their high efficiency in harvesting UV light[13], where CR quantum efficiency is highest[16], we explored the use of TiO_2 nanoparticles as a nanophotosensitizer (NPS) for CR-induced therapy (CRIT).

Synthesis and characterization of nanophotosensitizers (NPS)

Three types of stable TiO_2 NPS were synthesized for this study. The first NPS, polyethyleneglycol (PEG)-coated TiO_2 (TiO_2-PEG), was prepared by ultrasonicating TiO_2 with PEG (Molecular Weight: 400 Da), which transformed the TiO_2 nanoparticle aggregates into small nanoclusters (Fig. 1c and Table 1)[17]. Because this NPS is not designed to selectively target tumours through active transport system, it was used to determine tumour response to CRIT *via* intratumoural administration route, thereby minimizing undue liver and spleen organ toxicity caused by nonspecific uptake.

The second NPS, apo-transferrin (devoid of iron and abbreviated as Tf)-coated TiO_2 (TiO_2-Tf), was designed for intravenous (i.v.) administration and tumour-selective delivery. Many tumours overexpress Tf receptors because of the high demand for iron by rapidly proliferating cells[18]. We discovered that treatment of TiO_2 nanoclusters (Fig. 1c) with Tf produces stable, monodispersed TiO_2 NPS (Fig. 1c). At high concentrations of Tf, sonication facilitates adsorption of negatively charged Tf (isoelectric point = 5.5) onto TiO_2 (isoelectric point = 5.8) under neutral pH, which stabilizes the monodispersed NPS through protein-protein electrostatic repulsions. Although bovine serum albumin was previously used to prepare stable suspensions of TiO_2 nanoclusters in protein rich media[19], our new method allows Tf to serve simultaneously as TiO_2 monodispersant, stabilizer, and tumour targeting moiety.

To enhance and complement TiO_2 cytotoxicity with other sources of free radicals, we incorporated titanocene (Tc), a photoinitiator, into TiO_2 nanoparticles as the third NPS, (TiO_2-Tf-Tc). Tc belongs to the metallocene family and consists of two cyclopentadienyl

groups and two chlorides[20,21]. It has been used in phase II clinical trials as a chemotherapeutic drug, but the clinical trials were discontinued because of poor treatment outcomes[22,23]. Upon exposure to UV light, Tc spontaneously generates cyclopentadienyl and titanium-centred radicals (Fig. 1b) [24], a feature that is widely used in the plastics industry[20]. In aerated media, the free radicals are further converted to peroxyl radicals[25]. Because its excitation maximum is also in the UV region (λ = 250–325 nm; Supplementary Fig. 3b)[13,26], which favours CRIT, the photofragmentation of sub-cytotoxic doses of Tc will generate a different class of cytotoxic free radicals that could complement those from TiO_2 NPS, thereby augmenting cell death.

Because Tc is known to bind Tf at the iron-chelating epitope with similar binding affinity as iron[27] the synthesis of TiO_2-Tf-Tc is simplified. Thus, treatment of TiO_2 with Tf spontaneously forms TiO_2-Tf, which readily binds Tc to generate TiO_2-Tf-Tc without loss of Tf tumour targeting affinity (Fig. 1c). During synthesis, the temperature of the solution was maintained between 50 and 55°C to prevent denaturation of Tf at 60°C. Transmission electron microscopy (TEM) and dynamic light scattering (DLS) analyses confirmed the monodispersity (polydispersity index = 0.08) of TiO_2-Tf and TiO_2-Tf-Tc nanoparticles, with an average size distribution of 18±3 nm and hydrodynamic diameter of 106±18 nm (Table 1; and Supplementary Fig. 1, 2 in the Supplementary Information for additional characterization of the NPS, including the use of energy-dispersive X-ray spectroscopy, electron diffraction analysis and serum stability). Using the strong luminescence of TiO_2 in the visible region (Supplementary Fig. 3d), we observed CR-mediated TiO_2 luminescence in copper-64 (^{64}Cu; a β particle emitter) treated samples, but not in technetium-99m (a pure γ emitter) samples, demonstrating that CR is an effective excitation source for TiO_2 luminescence (Supplementary Fig. 3e). This finding is supported by a previous study that shows CR from phosphorous-32 can excite TiO_2 and cleave deoxyribonucleic acid (DNA)[28] in similar manner as activation with white light[29].

Cellular internalization of NPS and *in vitro* CRIT

TEM revealed endo-lysosomal localization of the TiO_2-Tf NPs in established human fibrosarcoma (HT1080) cells (Fig. 2a). Competitive inhibition of TiO_2-Tf internalization in tumour cells using saturating amounts of holo-Tf (iron-chelated Tf; Fig. 2b, c) demonstrates specific Tf-mediated endocytosis. However, attempts to reproduce this result *in vivo* only showed noticeable but statistically insignificant reduction in tumour uptake of the NPS (Supplementary Fig. 4). We attribute this finding to several factors, including the high turnover rate of Tf receptor after endocytosis, difficulty in saturating Tf receptor *in vivo* with saturating dose of Tf, and the high avidity of the TiO_2-Tf adduct.

TiO_2 NPS and Tc are known to induce apoptosis in cells at concentrations ≥ 5 μg/ml and 12.5 μg/ml, respectively[30,31]. To delineate intrinsic from CR-mediated toxicity, we used TiO_2-Tf, Tc-Tf, and TiO_2-Tf-Tc constructs at concentrations below the intrinsic cytotoxic threshold and induced CR with either ^{18}F or ^{64}Cu (Supplementary Fig. 5). With a half-life of 1.83 h and predominant β decay (β^+: 97%), FDG is suitable for systemic administration, where its high specific activity and tumour-targeting capability[32] combine to deliver rapid and localized CR for CRIT without prolonged radioactivity exposure to healthy tissue.

Under conditions where extended CRIT is needed, we used ^{64}Cu, which has a half-life of 12.7 h and significant β decay (β^+:19%, β^-:39%).

Treatment of NPS-loaded tumour cells with either FDG or ^{64}Cu, significantly decreased cell viability (Fig. 3a), and attenuated cell viability in a dose-dependent manner (Fig. 3b). By using a gelatinous mixture of structural proteins (Matrigel) to prevent the internalization of TiO_2 into cells, we demonstrate that the cells, with extracellular TiO_2, treated with ^{64}Cu remained viable (Fig. 3c; green), compared to the predominantly dead cells found in cells with intracellular TiO_2 (Fig. 3d). This could be attributed to a variety of factors, including the very short lived and short ranged characteristics of these radicals, which can react with structural proteins in Matrigel before they can damage tumour cells. Subcellular analysis of cells treated with alkaline comet assay shows various degrees of DNA mobility outside the nucleus (Fig. 3e). A significant percent of treated cells exhibited DNA damage, which correlated with the cell viability studies (Fig. 3f). Compared to normal and untreated cells (Fig. 3g), TEM images of TiO_2-Tf loaded cells after treatment with FDG reveal the loss of cell membrane integrity and vacuolated cytosol, features associated with necrosis (Fig. 3h). Morphologic changes such as dense nuclei, chromatin margination, and excessive surface blebbing, which indicate apoptosis, were also observed (Fig. 3i). However, cells treated with Tc-Tf and FDG exhibited predominantly apoptotic features (Fig. 3j). These results suggest that internalization of both NPS and the radionuclide in cells is a prerequisite for CR-induced cytotoxicity, affording CRIT a high degree of selectivity, precision, and control in a spatiotemporal setting.

Using dyes that are sensitive to hydroxyl and peroxyl radicals (hydroxyphenyl fluorescein, HPF)[33], and superoxide radicals (Mitosox), we demonstrate that cells treated with TiO_2-Tf and ^{64}Cu exhibited high levels of both HPF and Mitosox fluorescence (Fig. 3k). These results suggest the involvement of both hydroxyl and superoxide species in CRIT. While the free radicals involved in TiO_2 cytotoxicity are well established[34], the identification of free radicals and mechanism of cell death involved in photoinduced Tc mediated cell death is largely underexplored. We investigated potential changes to cell membranes in the form of lipid peroxidation, which is a hallmark of peroxyl radical induced damage, using an oxidation-sensitive ratiometric fluorescence probe, BODIPY® 581/591 C11. While coincubation of Tc-Tf with FDG induced significant peroxidation and degradation of cellular lipids, addition of peroxyl radical scavengers such as Trolox, adequately inhibited this process (Fig. 3l). This suggests that the free radicals with longer range and half-lifetime such as superoxide radicals from TiO_2 photocatalysis and peroxyl radicals from Tc photofragmentation are primarily responsible for inducing apoptosis during CRIT (see Supplementary Fig. 6, 7 and Supplementary Discussion for additional information).

In vivo CRIT

To demonstrate the *in vivo* application of CRIT, we administered intratumourally a single sub-cytotoxic dose of TiO_2-PEG NPS (2.5 μg/ml) and ^{64}Cu (0.5 mCi/0.1 ml) into aggressive HT1080 tumours in mice. The prolonged intratumoural retention (>4 days) of the non-tumour targeting TiO_2-PEG NPS and the long half-life of ^{64}Cu ensures extended CRIT without associated liver toxicity caused by nonspecific uptake. HT1080 tumours are viable

hypoxic tumour models[35], which is useful for testing and validating the oxygen independent mechanism of CRIT *in vivo*. We observed a remarkable shrinkage of the tumour volume (40±5%) within 3 days of CRIT initiation (Fig. 4a,b). Complete tumour regression was achieved by 30 days (Fig. 4b), translating into complete remission without significant loss in body weight up to 4 months post treatment (Supplementary Fig. 8). In contrast, the untreated HT1080 tumours grew rapidly and the mice were euthanized by day 15. Histologic analysis showed that the untreated tumour had the typical herringbone appearance characteristic of fibrosarcomas (Fig. 4c), but treated tumours revealed extensive necrosis at 72 h post-treatment (Fig. 4d).

Although intratumoural administration of drugs is a viable adjuvant therapy for a variety of tumours such as liver (radionuclide therapy through chemoembolization) or brain cancers, i.v. administration of both the NPS and radionuclide will expand the application of CRIT for the treatment of diverse primary and metastatic tumours. However, a major impediment to i.v. administration of nanoparticles is their high uptake in healthy liver, kidneys, and spleen relative to tumours. To determine the selective distribution and tumour-selective uptake of TiO_2-Tf NPS before CRIT, we prepared the fluorescent analogue of TiO_2-Tf by replacing the Tf with Alexa 680 fluorescent dye labelled holo-Tf (AlexaTf) to afford TiO_2-AlexaTf for *in vivo* and *ex vivo* optical imaging studies. At 24 h post injection, both tumour-targeted AlexaTf (Fig. 5a,b,e) and TiO_2-AlexaTf (Fig. 5c,d,e) exhibited tumour-to-liver fluorescence ratio of about 1.3 and 7.5, respectively, compared to the liver. In contrast, the intrinsic fluorescence from the non-Tf coated TiO_2-PEG displayed the conventional distribution profile of nanoparticles, with a poor tumour-to-liver fluorescence ratio of 0.2 (Fig. 5e). The uptake was highest in tumours for TiO_2-AlexaTf relative to other organs, an outcome that is rare for most nanoparticles (Fig. 5e). The high tumour-to-muscle ratio of 9.5 for TiO_2-AlexaTf (Fig. 5d, e) and the low uptake by liver, kidney, and spleen could be attributed to Tf-mediated endocytosis of the nanoparticles. Tf receptor has a fast turnover rate[36], enabling multiple cycles of endocytosis of circulating nanoparticles in the tumour.

To determine internalization of the non-fluorescent TiO_2-Tf-Tc constructs in tumour cells after systemic administration, we employed TEM for the *ex vivo* analysis of tumour sections The TEM images of tumour sections clearly show TiO_2 nanoparticles as dark spots in the cells, demonstrating the tumour uptake of the TiO_2-Tf-Tc NPS in majority of the cells and the retention of monodispersity *in vivo* (Fig. 5f). In addition to Tf-mediated endocytosis, the monodisperse, small size, and favourable surface properties of the Tf adducts probably facilitated the tumour uptake *via* enhanced permeability and retention (EPR) effect. The fractional contribution of EPR and avidity effects could be gleaned from the differences in the tumour-to-muscle ratio of 5.3 for Tf alone, which is much lower than that of TiO_2-Tf (Fig. 5b, e). In contrast to Tf-facilitated endocytosis, the tumour cells did not appear to internalize TiO_2-PEG aggregates *in vivo* (Fig. 5g), suggesting that the observed peritumoural uptake of these particles was primarily mediated by EPR effect. Therefore, a combination of both extracellular (EPR) and intracellular (Tf) processes accounts for the higher accumulation of TiO_2-Tf-Tc in the tumour environment than TiO_2-PEG nanoparticles.

The high tumour uptake of Tf-based products enabled a direct assessment of CRIT using a one-time dose of i.v. administered TiO_2-Tf, Tc-Tf and TiO_2-Tf-Tc (1 mg/kg body weight)

and two doses of FDG (0.87 mCi (32.19 MBq)/0.1 ml) within 72 h into separate mice bearing HT1080 tumours. We observed that the tumour growth rate for the mice undergoing CRIT was considerably slower than those in untreated or other control mice (Fig. 6a). The average tumour volume for mice treated TiO_2-Tf or Tc-Tf and mice FDG was four-fold smaller than the corresponding controls at day 15, when the control groups had to be euthanized before the tumour size attained 2 cm endpoint. Importantly, mice treated with TiO_2-Tf-Tc and FDG showed superior response to CRIT, with an eight-fold smaller average tumour volume compared to the control groups. The median survival increased from 15±2 d, for the untreated and control groups, to 30.5 d for TiO_2-Tf+FDG, 31 d for Tc-Tf+FDG, and a remarkable 50 d for TiO_2-Tf-Tc+FDG (Fig. 6b) treated mice. This result suggests that CR generated disparate cytotoxic free radicals from TiO_2 and Tc for complementary CRIT effect. We also observed the attenuation of tumour growth and significant increase in median survival to 21 d for TiO_2-Tf+FDG, 22 d for Tc-Tf+FDG, and 29 d for TiO_2-Tf-Tc +FDG, when treated with lower dose of FDG (0.43 mCi (15.91 MBq)/0.1 ml) than the 0.87 mCi described above (Fig. 6c). However, substitution of FDG with external UV light irradiation did not inhibit tumour growth (Fig 6a, b), probably due to the limited penetration of UV light (< 0.5 mm) across intact skin.

Extension of the treatment strategy to a slow growing non-small cell lung cancer tumour model, A549, showed a similar inhibition pattern of tumour growth (~ 6.5 fold at day 30) as HT1080 tumour model using TiO_2-Tf-Tc constructs (Fig. 6d), illustrating the potential application of the method to diverse tumour types. Taken together, the systemic and intratumoural CRIT data suggest positive correlation between *in vivo* cell death and the intensity of CR. Other factors such as duration of exposure determined by half-lives of radionuclides, administered dose, and type of radionuclide used will influence CRIT outcomes.

Our results show that i.v. administration of tracer amounts of FDG (0.14 mCi (5.18 MBq)/0.1 ml activity) and any of the Tf adducts did not induce CRIT (Fig. 6c), an observation that favours the dual role of FDG for imaging or CRIT. This outcome enabled the use of trace level FDG as a reporter of treatment response without inducing CRIT (Fig. 6e). After escalating the injected dose to > 0.4 mCi (15.91 MBq)/0.1 ml per mouse to trigger CRIT, FDG-PET imaging clearly demonstrates remarkable decrease in FDG uptake in tumours that responded to CRIT (Fig. 6e,f). Histological analysis of tumour sections of TiO_2-Tf and TiO_2-Tf-Tc treated mice reveal selective destruction of proliferating cells in the tumour region as well as pronounced necrotic zones occupying approximately 30% and 40% of the tumour mass, respectively (Fig. 6g). A significantly high number of tumour infiltrating lymphocytes (TIL), primarily neutrophils, and macrophages were observed among necrotic cells. Large areas of FDG and TiO_2-Tf or TiO_2-Tf-Tc treated tumours exhibited loss of cellular architecture, probably due to the scavenging of the necrotic debris by macrophages, as evidenced by large denuded pockets. In contrast, only 15% of the tumour mass in FDG and Tc-Tf treated mice, was necrotic, with a high TIL population showing a significantly higher distribution of apoptotic foci (Fig. 6g). These findings suggest that both free radicals and immune system activation against tumour cells through TIL recruitment mediated damage to cells. As observed in our *in vitro* studies, it appears that

necrosis is the dominant feature of TiO_2 based CRIT whereas apoptosis (see Fig. 3i,j) mediates cell death for the Tc based constructs. The extended median survival in TiO_2-Tf-Tc treated mice arises from the combined effects of different radicals generated by TiO_2 and Tc of the NPS. Comparison of untreated (Fig. 6h) and treated (Fig. 6i) tumour sections using TEM shows predominantly apoptotic cells in the latter. The localization of TiO_2-Tf based constructs in the apoptotic (Fig. 6j) and necrotic (Fig. 6k) cells also confirms the selectivity of the method.

Off-target toxicity is a concern for the i.v. based CRIT. This is particularly important in the liver and the kidneys, which are the main elimination route for the materials. These organs are also sensitive indicators of systemic toxicity caused by therapeutic interventions. Histological analysis of the liver and kidneys following CRIT did not show any significant lesions in the organs, indicating selective CRIT in proliferating tumour cells (Supplementary Fig. 9).

Conclusion

In this study, we have demonstrated a new approach to use CR from clinical grade PET radionuclides to photoactivate low radiance responsive targeted NPS for phototherapy. Combined effects of complimentary radical generation mechanisms of photocatalysts (hydroxyl and superoxide radicals) and photoinitiators (photofragmentation) enabled effective CRIT using tumour targeted NPS. The astute use of Tf as a tumour-targeting agent, Tc chaperone, TiO_2 chelator, a linker, and a dispersant to prevent nanoparticle aggregation, ushers a modular approach for NPS design and efficient tumour-targeted CRIT *in vivo*. FDG is widely used to detect diverse tumours with exceptionally high sensitivity because it accumulates in highly proliferating tumour cells undergoing enhanced glucose metabolism. Although it equally accumulates in non-tumour associated pathologies such as inflammation, CRIT is only effective when both CR source and NPS are in the same cell, which minimizes off target toxicity. The use of orthogonal tumour targeting mechanisms, where Tf and FDG internalize *via* Tf and GLUT1 receptors, respectively, prevents depletion of the targeted biomarkers prior to CRIT. While optimization of the dosing regimen with ^{18}F and ^{64}Cu could lead to complete tumour remission, employing β emitters such as Yttrium-90 (^{90}Y) with higher energy (2280 keV) than ^{18}F (633 keV) and ^{64}Cu (574 keV) would increase the UV light intensity of CR and further enhance CRIT effect. Because of the established biocompatibility of all components used in the study, our work creates a path to human translation. Although we focused on tumour therapy, the approach described in this study is versatile, opening the possibility of treating a variety of lesions in a depth- and oxygen-independent manner, thus overcoming the Achilles heel of phototherapeutic interventions.

Methods

Synthesis of TiO_2-PEG, TiO_2-Tf, Tc-Tf and TiO_2-Tf-Tc

Anatase TiO_2 (1 mg; Sigma Aldrich Co., St. Louis, MO, USA) was suspended in deionized water (1 ml) to prepare working stock solution. PEG 400 (100 μl) was added to the TiO_2 solution and sonicated using a probe sonicator for 10 min at room temperature (RT). The

mixture was then dialyzed overnight against Dulbecco's Phosphate Buffered Saline (DPBS) using a 3000 Da molecular weight cutoff Slide-A-Lyzer MINI Dialysis Devices (Thermo Fisher Scientific Inc., Waltham, MA, USA) to remove excess PEG. Working stock solutions of Tf were prepared by dissolving 5 mg of human apo-Tf (Sigma Aldrich Co.) in 1 ml DPBS, pH 7.4. To prepare TiO_2-Tf, a 1:1 (v/v) solution of TiO_2 and Tf was mixed and probe sonicated in continuous mode for ~ 2 min. It is important to ensure the temperature of the solution does not exceed 55°C to prevent denaturation of Tf (60°C). The solution was then immediately passed through a 0.45 μm syringe filter to isolate monodisperse nanoparticles. To prepare Tc-Tf, five-fold molar excess of Tc (Sigma Aldrich Co.) was added to human apo-Tf and incubated in a shaker for 2 h at room temperature (RT). A working stock of Tc was initially prepared in DMSO due to low solubility of Tc in water and aqueous buffers. The mixture was then dialyzed overnight against DPBS using a 3000 Da molecular weight cutoff Slide-A-Lyzer MINI Dialysis Devices to remove excess Tc. TiO_2-Tf-Tc was similarly prepared by incubating Tc with TiO_2-Tf conjugates and thereafter dialyzed to remove excess Tc.

Physicochemical Characterization

TEM images of TiO_2 based constructs were acquired using a FEI Tecnai Spirit Transmission Electron Microscope (FEI, Hillsboro, OR, USA) operating at an acceleration voltage of 200 kV. EDX and electron diffraction analysis was performed using a JEOL 2000FX TEM (JEOL USA Inc., Peabody, MA, USA) and Philips EM420 TEM@120Kv (TEM Analysis Service Lab, Azle, TX, USA). TEM grids coated with a layer of formvar were used throughout these studies. Dynamic light scattering measurements were acquired with a Malvern Zetasizer Nano ZS (Malvern Instruments Ltd., Malvern, UK) instrument equipped with a 633 nm laser. Three measurements were conducted for each sample with at least 10 runs and each run lasting 10 s. All sizes reported were based on intensity average. Absorption spectra of TiO_2 and Tc were recorded on a Beckman Coulter DU 640 UV-visible spectrophotometer (Beckman Coulter Inc., Brea, CA, USA) and analysed using Graphpad Prism statistical software. Fluorescence spectra of TiO_2 were recorded on a Fluorolog-3 spectrofluorometer (Jobin Yvon Horiba, Kyoto, Japan). The sample was placed in a quartz cuvette and measurements recorded in triplicates.

Cell culture

All cell lines were purchased from American Type Culture Collection (ATCC, Manassas, VA, USA) that underwent STR profiling and tested for mycoplasma contamination. HT1080 fibrosarcoma cell line was cultured under recommended standard conditions. HT1080 cells were cultured in Dulbecco's Modified Eagle's Medium containing 10% foetal bovine serum (FBS), L-glutamine (2 mM), penicillin (100 units/ml), and streptomycin (100 μg/ml), incubated at 37°C in a humidified atmosphere of 5% CO_2 and 95% air. For cytotoxicity studies, a concentration of 2.5 μg/ml of the TiO_2-Tf, Tc-Tf, and TiO_2-Tf-Tc constructs as well as 0.2, 0.4 and 0.85 mCi/0.1 ml of FDG; and 0.5 mCi/0.1 ml ^{64}Cu were used. Randomized block design was used for all *in vitro* experiments, which were run in triplicates, by dividing them into three blocks for all the treatment groups.

In vitro cell viability assays

MTS (3-(4,5-dimethylthiazol-2-yl)-5-(3-carboxymethoxyphenyl)-2-(4-sulfophenyl)-2H-tetrazolium) assay, a calorimetric assay for assessing viability of cell culture, was performed using CellTiter 96 AQ_{ueous} Non-Radioactive Cell Proliferation Assay kit (Promega Co., Fitchburg, WI, USA) according to the manufacturer's instructions. The cells were incubated with the constructs and FDG for 48 h before analysis.

Alkaline comet assays (Cell Biolabs Inc., San Diego, CA, USA) were performed using the manufacturer's protocol. Briefly, treated and untreated control cells were removed from flask by scraping with a rubber policeman. The cell suspension was centrifuged and washed with ice-cold DPBS two times and re-suspended at 1×10^5 cells/ml in ice-cold DPBS. Cells were embedded in low melt Comet agarose and plated on provided microscope slides. The cells were then lysed with lysis buffer and treated with alkaline solution. The slides were electrophoresed in alkaline solution at 1 V/cm with a setting of 300 mAmp for 30 minutes. The slides were stained with Vista Green DNA dye after washing and drying. Fluorescence images were acquired using an Olympus BX51 epifluorescence microscope equipped with a charge coupled device camera. % Tail DNA was estimated using OpenComet (v1.3) plugin for Image J software.

TEM analysis of cells and tissue with TiO_2-Tf and Tc-Tf

For ultrastructural analysis, cells and tissue samples were fixed in 2% paraformaldehyde/2.5% glutaraldehyde (Polysciences Inc., Warrington, PA, USA) in cacodylate buffer (100 mM, pH 7.2) for 1 h at room temperature. Samples were washed in cacodylate buffer and postfixed in 1% osmium tetroxide (Polysciences Inc.) for 1 h. Samples were then rinsed extensively in distilled water before en bloc staining with 1% aqueous uranyl acetate (Ted Pella Inc., Redding, CA, USA) for 1 h. Following several rinses in water, samples were dehydrated in a graded series of ethanol and embedded in Eponate 12 resin (Ted Pella Inc.). Sections of 95 nm were cut with a Leica Ultracut UCT ultramicrotome (Leica Microsystems Inc., Buffalo Grove, IL, USA), stained with uranyl acetate and lead citrate, and viewed on a JEOL 1200 EX transmission electron microscope (JEOL USA Inc.) equipped with an AMT 8 megapixel digital camera (Advanced Microscopy Techniques, Woburn, MA, USA).

In cellulo receptor binding

We used Tflabelled with Alexa 680 (AlexaTf; Life Technologies, Carlsbad, CA, USA) to prepare fluorescent TiO_2-AlexaTf construct, and the products were processed as described above. HT1080 cells were grown in 8 well chamber slides and incubated with TiO_2-AlexaTf, final concentration of 0.25 mg/ml, and incubated for 1 h at 37°C. For Tf blocking, 25 mg/ml (100 X) of holo-Tf (Sigma Aldrich Co.) was added and incubated for 1 h before adding TiO_2-AlexaTf. The wells were washed 3X before imaging. Fluorescence images were acquired using an Olympus FV1000 confocal microscope. Fluorescence/brightfield cell images were taken with a 60X objective using a He:Ne 633 nm excitation laser and emission range of dichroic mirror set to 655–755 nm. Fluorescence and brightfield image overlay with false colour was performed using Fluoview FV10-ASW software from Olympus (Center Valley, PA, USA). One hundred cells per well were counted to quantify fluorescence intensity.

In cellulo Hydroxyl and Superoxide radical assay

Hydroxyphenyl fluorescein (HPF) with an excitation and emission wavelength of 490 nm and 515 nm, respectively (Life Technologies Inc.) was used according to the manufacturer's instructions. Briefly, the 5 mM stock was diluted 1,000X to prepare 5 μM working stock solution in DPBS. The TiO_2-Tf, Tc-Tf and TiO_2-Tf-Tc and FDG treated HT1080 cells grown in 8 well culture slides were immersed in the HPF working stock 4 h post treatment. The cells were incubated for 1 h before the dye solution was removed and replaced with fresh DPBS. The cells were imaged by confocal microscopy using the 488 nm Argon ion laser with emission set to 500–600 nm. Similarly, Mitosox Red (Life Technologies Inc.) with an excitation and emission wavelengths of 510 nm and 580 nm, respectively, was used to detect superoxide radicals according to the manufacturer's instructions.

Lipid peroxidation and mitochondrial membrane potential assay

BODIPY® 581/591 C11 reagent (Life Technologies Inc.) was used to quantitatively determine the degree of lipid peroxidation. It is a ratiometric fluorescence technique that relies on oxidation of lipids to shift fluorescence emission peak from 590 nm to 510 nm. HT1080 cells (~10,000) were grown in 96 well plate and incubated with Tc-Tf (2.5 μg/ml) and FDG (0.85 mCi/0.1 ml) for 6 h. Peroxyl radical scavenging was performed by coincubating Tc-Tf+FDG with Trolox (1 mM), a water soluble analogue of Vitamin E and a powerful antioxidant. As positive control, 2, 2'-azobis-2-methyl-propanimidamide, dihydrochloride (AAPH; 100 μM) was used. All the compounds were incubated for 6 h at 37°C. Finally, the BODIPY-based dye (10 μM) was added and incubated for 30 min at 37°C. After washing the cells with PBS three times, the plate was analysed using a Synergy HT multimode plate reader (BioTek Instruments Inc., Winooski, USA) with excitation/emission of 581/591 nm for the reduced dye and at 488/510 nm for the oxidized dye. The ratio of the fluorescence intensities at 590/510 nm was plotted to derive the ratio of fluorescence change.

For measuring mitochondrial membrane potential, Mitotracker Green (Life Technologies Inc.) was used according to manufacturer's instructions. Staurosporine (2 μM; Sigma Aldrich Co.) was used as positive control. Fluorescence readout was performed using a plate reader using excitation/emission wavelengths of 490/516 nm.

Matrigel based cell studies

Matrigel™ (BD Biosciences, San Jose, CA, USA) was thawed at 4°C. For entrapment of NPS, we first mixed an equal volume of TiO_2 NPS solutions (3 mg/ml) with Matrigel, which was then plated on 8 well chamber culture slides. HT1080 cells were then introduced on the slides and allowed to grow in Matrigel. Since Matrigel solidifies at 37°C, TiO_2 NPS remain suspended and immobilized in the gel and are not internalized by the surrounding cells. For the internalization model, Matrigel was omitted and cells were incubated with TiO_2 NPS to facilitate internalization. The cells were then washed to remove non-internalized TiO_2 NPS and reseeded on chamber slides. ^{64}Cu (0.5 mCi/0.1 ml) was then added to the respective chambers with (extracellular TiO_2) and without (intracellular TiO_2) matrigel and incubated for 48 h at 37°C before performing the Live/Dead assay (Life Technologies Inc.) according to the manufacturer's instructions.

Chelation of ^{64}Cu to DOTA

For experiments with ^{64}Cu, we prepared a stock solution (1 mg/ml) of DOTA (1,4,7,10-tetraazacyclododecane-1,4,7,10-tetraacetic acid; Macrocyclics Inc., Dallas, TX, USA) in ammonium acetate buffer (50 mM) equilibrated to pH 5.5. Aliquots of DOTA stock solution (50 μl) was added to ammonium acetate buffer (450 μl), followed by ^{64}Cu (5 mCi; 185 MBq) in 0.1 M hydrochloric acid (5 μl). The reaction mixture was incubated at 45°C for 1 h in a shaker. Non-chelated ^{64}Cu was removed from the chelated DOTA-^{64}Cu using a Waters HPLC purification system. The flow rate was set to 1 ml/min. The solvents were A: 0.1% trifluoracetic acid (TFA) in water, and B: 0.1% TFA in acetonitrile. After 5 min hold at 5% B, the gradient was programmed linearly to 100% B at 40 min. The sample eluted at 6 min post injection, corresponding to the peak in the radiometer and UV detector. The sample was then dried in a rotary shaker to remove TFA and acetonitrile before re-suspending the residue in DPBS.

In vivo tumour model

Athymic nu/nu mice (8 week, female) were purchased from Frederick Cancer Research and Development Center (Frederick, MD, USA). All studies were conducted in compliance with Washington University Animal Welfare Committee's requirements for the care and use of laboratory animals in research. The HT1080 xenografts were generated by subcutaneous injection of 4×10^6 cells in DPBS (100 μl) in both flanks of Athymic nude mice. Likewise, a bilateral subcutaneous tumour model of A549 was developed using 5×10^6 cells in DPBS.

In vivo Biodistribution studies

Athymic nude mice (8 week, female) with a tumour volume of ~ 300 mm^3, were injected with 3.2 mg/ml (12.8 mg/kg) of TiO_2-AlexaTf (n = 5) and AlexaTf (n = 5) (Life Technologies Inc.) in DPBS (100 μl) intravenously through the lateral tail vein. Fluorescence imaging was performed using excitation and emission wavelengths of 685nm and 720 nm, respectively, in a Pearl whole animal imager (Li-Cor Biosciences Inc., Lincoln, NE, USA). The mice were euthanized 24 h post-injection and the major organs were dissected and imaged. Mean fluorescence intensity for each tissue was estimated by region of interest analysis using Pearlcam software (Li-Cor Biosciences Inc.). The intensity was normalized to equalize muscle fluorescence levels and plotted for all the organs. For TiO_2 alone, the mice were injected with 250 μg/ml of TiO_2-PEG in DPBS (100 μl) intravenously through tail vein. The organs were dissected and fluorescence imaging was performed using Kodak IS4000MM multimodal imaging system (Carestream Health Inc., Rochester, NY, USA) with excitation/emission wavelength set to 640/700 nm, 60 s exposure with 2×2 binning, for detecting TiO_2 using its inherent fluorescence.

In vivo blocking studies

In Athymic nu/nu mice (8 week, female) bearing HT1080 tumours, 200 mg/kg of holo-Tf (Sigma Aldrich Co.) was administered i.v. After 45 min, TiO_2-AlexaTf (10 mg/kg) was administered, and imaging was performed as described above. The animals were euthanized 24 h post injection for *ex vivo* biodistribution analysis of the organs.

CRIT of solid tumours

For intratumoural administration, a cocktail of 2.5 μg/ml of TiO_2-PEG and 0.5 mCi/0.1 ml chelated ^{64}Cu in 50 μl of DPBS was injected directly into the tumour mass, after the tumour volume reached 200 mm^3. Two diametrically opposite injection sites were chosen and 25 μl of the cocktail was delivered at each site. Four groups (n = 4), TiO_2-PEG treated mice, ^{64}Cu treated mice, non-radioactive Cu (1 μM $CuCl_2$) treated mice and untreated mice, served as controls.

For systemic administration, when tumour volume reached 50 mm^3, the mice (n = 6 per group) were injected with 1 mg/kg TiO_2-Tf, Tc-Tf, TiO_2-Tf-Tc in 100 μl of DPBS intravenously followed by 0.87 mCi/0.1 ml of FDG, also intravenously, 24 h later. Control mice (n = 6 per group) were administered with DPBS, TiO_2-Tf, Tc-Tf, TiO_2-Tf-Tc or FDG alone. Animals were randomly divided into three blocks of two animals each for different treatments. Food was withheld from mice for 6 h before administering FDG and kept in a dark, lead-shielded room post injection until the activity decayed. A second administration of FDG (0.87 mCi/0.1 ml) was given 48 h after the first FDG injection. Similarly, two additional cohorts were administered with 0.14 mCi/0.1 ml and 0.43 mCi/0.1 ml FDG (n = 4 per group), respectively, and monitored over 45 d. For mice undergoing treatment using external UV light irradiation, the tumours were irradiated directly by a mercury lamp (300–400 nm) for l h at 14–20 J/cm^2, 24 h after administration of TiO_2-Tf-Tc constructs. Irradiation was reapplied again after 48 h and the cycle repeated 2X. For both, systemic and intra-tumoural studies, the mice were monitored for 45 days and the growing tumours were measured with callipers every two days and tumour volume calculated using the equation: $=(\text{length} \times \text{width}^2)/2$. The tumour volume was plotted versus time to analyse CRIT effect on the different groups of mice. The weight and any physical signs for distress were also monitored closely. The mice were euthanized by cervical dislocation after anaesthesia with 5% isoflurane when the tumour size reached 2 cm or loss of >20% total body weight. The mice with regressing tumours were monitored for an additional four months to determine whether the cancer was in remission. Similarly, CRIT was performed on slow growing A549 xenograft models and tumour growth was monitored for 35 days.

FDG-PET Imaging

FDG-PET imaging was performed on untreated mice on day 15 and on treated mice on day 30. The mice were fasted for 6 h before each scan and clinical grade FDG was obtained from the Washington University Cyclotron Facility. After anesthetizing the mice with 1.5–2% Isoflurane and Oxygen, 0.19 mCi (7.03 MBq)/0.1 ml of FDG was administered intravenously. Small animal PET imaging was performed at 1h post injection using Inveon MicroPET/CT scanner (Siemens, Knoxville, TN). A 10-minute transition scan was performed just before the10-minute static PET images were acquired. The images were registered with the image display software (Inveon Research Workplace, Siemens, Knoxville, TN). Using this software, the tumour region was contoured and the standard uptake values (SUVs) were calculated as follows: SUV = [(mCi/ml)×(animal weight (g))/(injected dose (mCi)].

Histology

The HT1080 tumour bearing mice in the control groups were euthanized 15 d post administration of TiO_2-Tf, Tc-Tf, TiO_2-Tf-Tc constructs or FDG, while mice treated with 1 mg/kg of TiO_2-Tf and Tc-Tf with FDG were euthanized 30 d post administration and the group treated with 1 mg/kg of TiO_2-Tf-Tc with FDG were euthanized at 45 d post administration. Similarly, mice treated by intratumoural administration of TiO_2-PEG and ^{64}Cu were euthanized for histology 3 d after treatment. The tumours were harvested and snap-frozen in Optimal Cutting Temperature (OCT) media for routine staining with haematoxylin and eosin (H&E). Brightfield images of H&E stained 10 μm tumour sections were obtained by epifluorescence microscopy at 4X and 20X magnifications.

Statistical analysis

Statistical significance was measured by Student's t-test using GraphPad Prism software (GraphPad, San Diego, CA). Kaplan-Meir survival curves were plotted using GraphPad Prism software. Unless noted otherwise, all values are means and error bars are standard deviations. For animal studies, sample size estimates depend on the effect size (mean difference between untreated and treatment groups/SD) of outcome. For effect size of 2.1 and using two-sided t-test, typically 5 per group were needed with 80% power to detect a significant difference at a type I error rate of 0.05.

Supplementary Material

Refer to Web version on PubMed Central for supplementary material.

Acknowledgments

Funding for this project was in part by grants from the US National Institutes of Health (NCI R01 CA171651 and P50 CA094056; NIBIB R01 EB008111, and SIG S10 RR031625) and the National Science Foundation (CCF 0963742). We thank Tom Voller and Paul Eisenbeis for generously providing ^{64}Cu; Vijay Sharma for technetium-99m; Wandy Beatty, Suellen Greco for analysing histology sections; Patrick Gibbons, Howard Wynder and Jeffrey Elsner for assistance with TEM imaging; and staff of Siteman Cancer Center Small Animal microPET Facility for imaging with FDG-PET.

References

1. Ethirajan M, Chen Y, Joshi P, Pandey RK. The role of porphyrin chemistry in tumor imaging and photodynamic therapy. Chem Soc Rev. 2011; 40:340–362. [PubMed: 20694259]
2. Spring BQ, et al. Selective treatment and monitoring of disseminated cancer micrometastases in vivo using dual-function, activatable immunoconjugates. Proc Natl Acad Sci U S A. 2014; 111:26.
3. Jelley JV. Cerenkov radiation and its applications. Br J Appl Phys. 1955; 6:227.
4. Robertson R, et al. Optical imaging of Cerenkov light generation from positron-emitting radiotracers. Phys Med Biol. 2009; 54:0031–9155.
5. Cherry, S.; Dahlbom, M. PET: Physics, Instrumentation, and Scanners. In: Phelps, M., editor. PET. Springer; New York: 2006. p. 1-117.
6. Liu H, et al. Molecular Optical Imaging with Radioactive Probes. PLoS ONE. 2010; 5:e9470. [PubMed: 20208993]
7. Spinelli AE, et al. Multispectral Cerenkov luminescence tomography for small animal optical imaging. Opt Express. 2011; 19:12605–12618. [PubMed: 21716501]

8. Kotagiri N, Niedzwiedzki DM, Ohara K, Achilefu S. Activatable Probes Based on Distance-Dependent Luminescence Associated with Cerenkov Radiation. Angew Chem Int Ed Engl. 2013; 52:7756–7760. [PubMed: 23765506]
9. Sun X, et al. Self-Illuminating 64Cu-Doped CdSe/ZnS Nanocrystals for in Vivo Tumor Imaging. J Am Chem Soc. 2014; 136:1706–1709. [PubMed: 24401138]
10. Axelsson J, Davis SC, Gladstone DJ, Pogue BW. Cerenkov emission induced by external beam radiation stimulates molecular fluorescence. Med Phys. 2011; 38:4127–4132. [PubMed: 21859013]
11. Spinelli AE, et al. First human Cerenkography. J Biomed Opt. 2013; 18:20502. [PubMed: 23334715]
12. Thorek DL, Ogirala A, Beattie BJ, Grimm J. Quantitative imaging of disease signatures through radioactive decay signal conversion. Nat Med. 2013; 19:1345–1350. [PubMed: 24013701]
13. Linsebigler A, Lu G, Yates J. Photocatalysis on TiOn Surfaces: Principles, Mechanisms, and Selected Results. Chem Rev. 1995; 95:735–758.
14. Schwarz PF, et al. A New Method To Determine the Generation of Hydroxyl Radicals in Illuminated TiO2 Suspensions. J Phys Chem B. 1997; 101:7127–7134.
15. Boehm HP. Acidic and basic properties of hydroxylated metal oxide surfaces. Discuss Faraday Soc. 1971; 52:264–275.
16. Mitchell GS, Gill RK, Boucher DL, Li C, Cherry SR. In vivo Cerenkov luminescence imaging: a new tool for molecular imaging. Philos Trans A Math Phys Eng Sci. 2011; 369:4605–4619. [PubMed: 22006909]
17. Huang W, Lei M, Huang H, Chen J, Chen H. Effect of polyethylene glycol on hydrophilic TiO2 films: Porosity-driven superhydrophilicity. Surf Coat Tech. 2010; 204:3954–3961.
18. Gatter KC, Brown G, Trowbridge IS, Woolston RE, Mason DY. Transferrin receptors in human tissues: their distribution and possible clinical relevance. J Clin Pathol. 1983; 36:539–545. [PubMed: 6302135]
19. Ji Z, et al. Dispersion and stability optimization of TiO2 nanoparticles in cell culture media. Environ Sci Technol. 2010; 44:7309–7314. [PubMed: 20536146]
20. Bowman DC. The Amazingly Versatile Titanocene Derivatives. J Chem Educ. 2006; 83:735.
21. Clearfield A, Warner DK, Saldarriaga-Molina CH, Ropal R, Bernal I. Structural Studies of (π-C5H5)2MX2 Complexes and their Derivatives. The Structure of Bis(π-cyclopentadienyl)titanium Dichloride. Can J Chem. 1975; 53:1622–1629.
22. Lümmen G, Sperling H, Luboldt H, Otto T, Rübben H. Phase II trial of titanocene dichloride in advanced renal-cell carcinoma. Cancer Chemother Pharmacol. 1998; 42:415–417. [PubMed: 9771957]
23. Kröger N, Kleeberg UR, Mross K, Edler L, Hossfeld DK. Phase II Clinical Trial of Titanocene Dichloride in Patients with Metastatic Breast Cancer. Oncol Res Treat. 2000; 23:60–62.
24. Davidenko N, Garcia O, Sastre R. The efficiency of titanocene as photoinitiator in the polymerization of dental formulations. J Biomater Sci Polym Ed. 2003; 14:733–746. [PubMed: 12903740]
25. Tehfe MA, Lalevée J, Morlet-Savary F, Graff B, Fouassier JP. On the Use of Bis(cyclopentadienyl)titanium(IV) Dichloride in Visible-Light-Induced Ring-Opening Photopolymerization. Macromolecules. 2011; 45:356–361.
26. Brindley PB, Davies AG, Hawari JAA. An ESR study of the photolysis of dicyclopentadienyltitanium dichloride. J Organomet Chem. 1983; 250:247–256.
27. Qian ZM, Li H, Sun H, Ho K. Targeted drug delivery via the transferrin receptor-mediated endocytosis pathway. Pharmacol Rev. 2002; 54:561–587. [PubMed: 12429868]
28. Tijana, R.; Nada, MD.; Adam, E.; Elena, R. Handbook of Nanophysics. CRC Press; 2010. Biofunctionalized TiO2- Based Nanocomposites; p. 1-28.
29. Paunesku T, et al. Biology of TiO2-oligonucleotide nanocomposites. Nat Mater. 2003; 2:343–346. [PubMed: 12692534]

30. Zhao J, et al. Titanium dioxide (TiO2) nanoparticles induce JB6 cell apoptosis through activation of the caspase-8/Bid and mitochondrial pathways. J Toxicol Environ Health A. 2009; 72:1141–1149. [PubMed: 20077182]

31. O'Connor K, et al. Novel titanocene anti-cancer drugs and their effect on apoptosis and the apoptotic pathway in prostate cancer cells. Apoptosis. 2006; 11:1205–1214. [PubMed: 16699961]

32. Kelloff GJ, et al. Progress and promise of FDG-PET imaging for cancer patient management and oncologic drug development. Clin Cancer Res. 2005; 11:2785–2808. [PubMed: 15837727]

33. Heyne B, Maurel V, Scaiano JC. Mechanism of action of sensors for reactive oxygen species based on fluorescein-phenol coupling: the case of 2-[6-(4′-hydroxy)phenoxy-3H-xanthen-3-on-9-yl]benzoic acid. Org Biomol Chem. 2006; 4:802–807. [PubMed: 16493462]

34. Rozhkova EA, et al. A high-performance nanobio photocatalyst for targeted brain cancer therapy. Nano Lett. 2009; 9:3337–3342. [PubMed: 19640002]

35. Misra RM, Bajaj MS, Kale VP. Vasculogenic mimicry of HT1080 tumour cells in vivo: critical role of HIF-1alpha-neuropilin-1 axis. PLoS ONE. 2012; 7:21.

36. Dautry-Varsat A, Ciechanover A, Lodish HF. pH and the recycling of transferrin during receptor-mediated endocytosis. Proc Natl Acad Sci U S A. 1983; 80:2258–2262. [PubMed: 6300903]

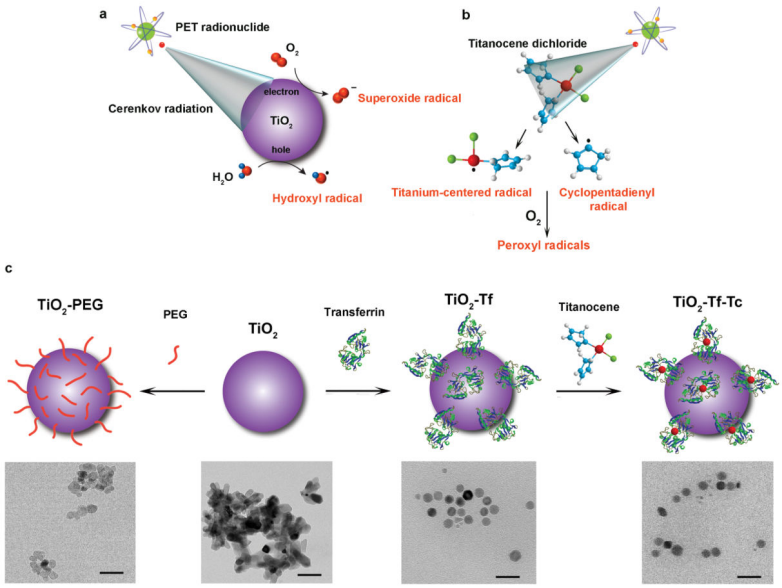

Figure 1. Titanium dioxide and Titanocene photoagents for CRIT

a, Schematic of CR mediated excitation of TiO_2 nanoparticles to generate cytotoxic hydroxyl and superoxide radicals from water and dissolved oxygen, respectively, through electron-hole pair generation. CR is generated by PET radionuclides (not to scale). **b,** Schematic of CR mediated excitation of Tc to generate a cyclopentadienyl radical and a titanium-centred radical through photofragmentation (not to scale). In aerated media, the radicals transform into more potent peroxyl radicals. **c,** Schematic illustrating the development of TiO_2-PEG,TiO_2-Tf by coating TiO_2 with Tf and subsequent generation of TiO_2-Tf-Tc construct by simple addition of Tc, which docks into the iron binding site of Tf (not to scale). Below (left to right) are the TEM images of TiO_2-PEG, TiO_2 aggregates, TiO_2-Tf and TiO_2-Tf-Tc (right). Scale bar, 50 nm. CR and NPS generate disparate and regenerative cytotoxic free radicals for CRIT.

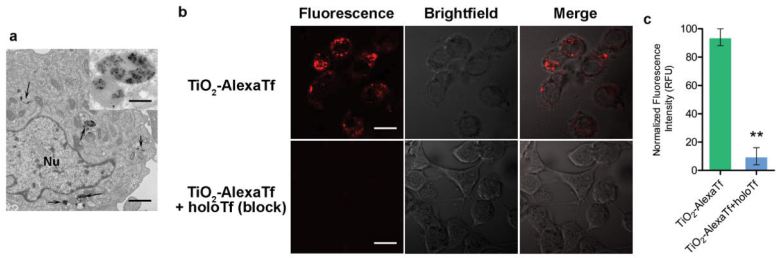

Figure 2. Cellular uptake of NPS

a, TEM image of a HT1080 tumour cell showing internalized and endo-lysosomal localization of the TiO_2-Tf constructs (arrows). Scale bar, 2 μm. Inset shows two lysosomal compartments with TiO_2-Tf. Scale bar, 400 nm. **b,** *In cellulo* uptake of TiO_2-AlexaTf and successful blocking with holo-Tf suggesting Tf receptor mediated internalization as the mechanism of uptake. Scale bar, 20 μm. **c,** Quantitation of successful blocking of TiO_2-AlexaTf internalization by saturating doses of holo-Tf in HT1080 cells. Values are means ± s.e.m. (experiments for each group were run in triplicates and replicated 2X). $^{**}P < 0.01$. Tf receptor mediates endocytosis of Tf-coated NPS in tumour cells.

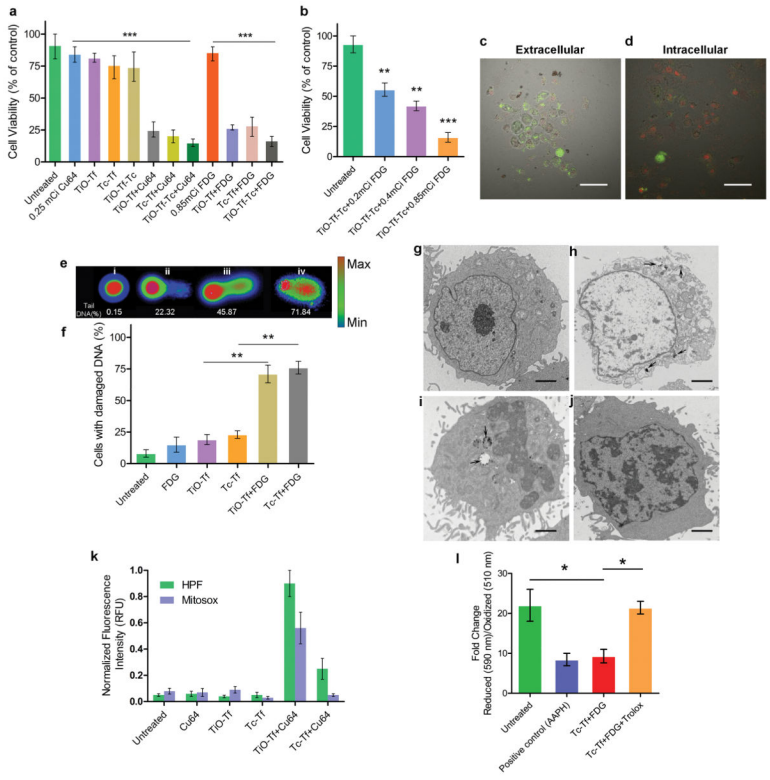

Figure 3. *In vitro* assessment of CRIT

a, Cell viability assay comparing the TiO_2-Tf, Tc-Tf and TiO_2-Tf-Tc constructs with and without exposure to ^{64}Cu and FDG on HT1080 cells. Values are means ± s.e.m. (experiments for each group were run in triplicates). ***$P < 0.001$. **b,** Cell viability assay using TiO_2-Tf-Tc with different activities of FDG demonstrating significant cell killing even at 0.2 mCi/0.1 ml. Values are means ± s.e.m. (experiments for each group were run in triplicates and replicated 3X). **$P < 0.01$, ***$P < 0.001$. **c,** Confocal microscopy image of merged bright-field and fluorescence images of Matrigel™ suspended cells with extracellular TiO_2 and **d,** intracellular TiO_2, with 0.5 mCi/0.1 ml ^{64}Cu. Live/Dead® cell viability stain was used to distinguish live cells (green) from dead cells (red). Scale bar, 50 μm. Experiments were replicated 3X. **e,** Examples of alkaline comet assay results. The images show undamaged and damaged DNA as a result of free radical damage and apoptosis. Image marked (i) is representative of undamaged DNA, from the controls, including untreated cells and either exposed to NPS or radionuclide alone. Notice there is negligible DNA in the tail (0.15%). In comparison, cells treated with the NPS and radionuclide, show considerable DNA damage as shown in (ii, iii, iv). Cells in the same treatment group exhibited variable DNA damage, such as 22.32%, 45.87% and 71.84% DNA in the tail. The fluorescence intensity is represented in pseudocolour. **f,** Cells undergoing CRIT demonstrated an overall higher percent of damaged DNA. 100 cells were counted from each group. Values are means ± s.e.m. **$P < 0.01$. Experiments were replicated 3X. **g,** TEM image of a normal HT1080 cell. Scale bar, 3 μm. **h,** TEM image showing a necrotic cell that was treated with TiO_2-Tf (arrows) and FDG. Notice loss of cell membrane integrity and highly vacuolated cytoplasm. Scale bar, 2 μm. **i,** TEM image

showing an apoptotic cell that was treated with TiO_2-Tf (arrows) and FDG. Notice surface blebbing and condensed chromatin. Scale bar, 1.4 μm. **j,** TEM image of an apoptotic cell that was treated with Tc-Tf and FDG. Notice nuclear fragmentation and chromatin margination. Scale bar, 1.4 μm. **k,** Comparison between HT1080 cells not undergoing and undergoing CRIT with TiO_2-Tf and Tc-Tf show higher output of free radicals such as hydroxyl, superoxide and peroxyl species as measured using HPF and Mitosox fluorescent dyes. Values are means ± s.e.m. (experiments for each group were run in triplicates and replicated 3X). **l,** Lipid peroxidation assay using BODIPY 581/591 C11 reagent on HT1080 cells showing higher degree of lipid peroxidation in cells treated with Tc-Tf and FDG. Values are means ± s.e.m (experiments for each group were run in triplicates and replicated 3X). *$P < 0.05$. Intracellular localization of both radionuclide and NPS is critical for effective CRIT.

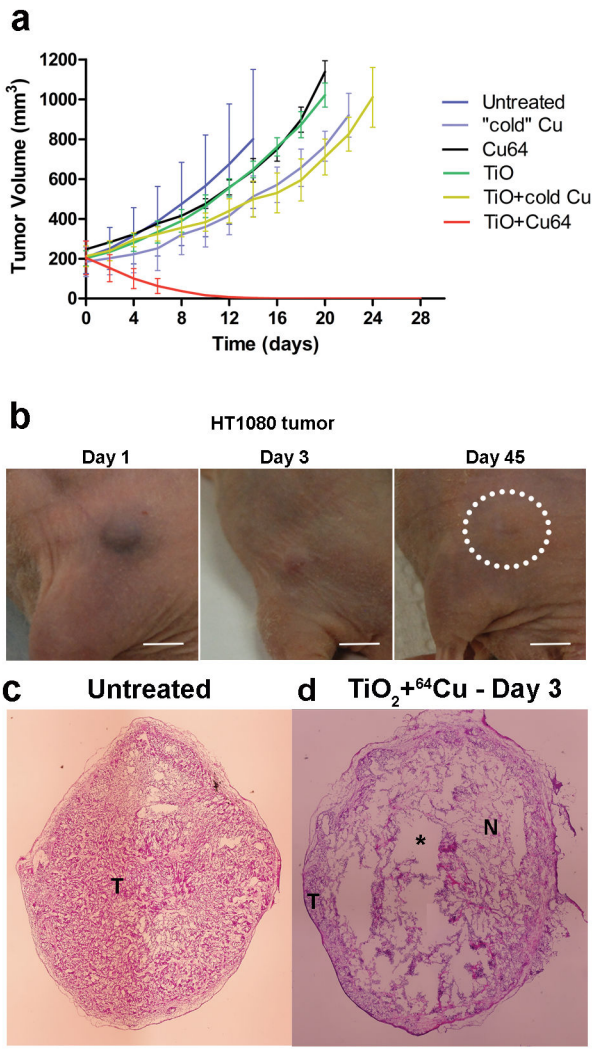

Figure 4. CRIT through intratumoural administration of TiO_2 and ^{64}Cu

a, *In vivo* CRIT through a one-time intratumoural administration of PEGylated TiO_2 and ^{64}Cu in HT1080 tumour bearing Athymic nu/nu mice. Toxicity through elemental Cu was eliminated by using non-radioactive $CuCl_2$, with and without TiO_2-PEG. Values are means ± s.e.m. (n = 4 mice per group). Experiments were replicated 2X. **b,** Representative photographs at day 1, 3 & 45 of HT1080 tumour bearing mice injected with a single dose of 2.5 μg/ml of TiO_2-PEG and 0.5 mCi/0.1 ml of ^{64}Cu intratumourally at day 1. Scale bar, 5 mm. Complete tumour elimination was achieved after PDT at day 45 (dotted circle). **c,** H&E stained HT1080 tumour section before PDT showing typical herringbone architecture of fibrosarcoma. Scale bar, 1 mm. (n = 4 histological sections per group). **d,** H&E stained HT1080 tumour section 3 d after commencement of PDT showing extensive necrotic centres and destruction of the tumour architecture. Scale bar, 1 mm. (n = 4 histological sections per group). CRIT can achieve tumour remission through intratumoural administration of both radionuclide and NPS.

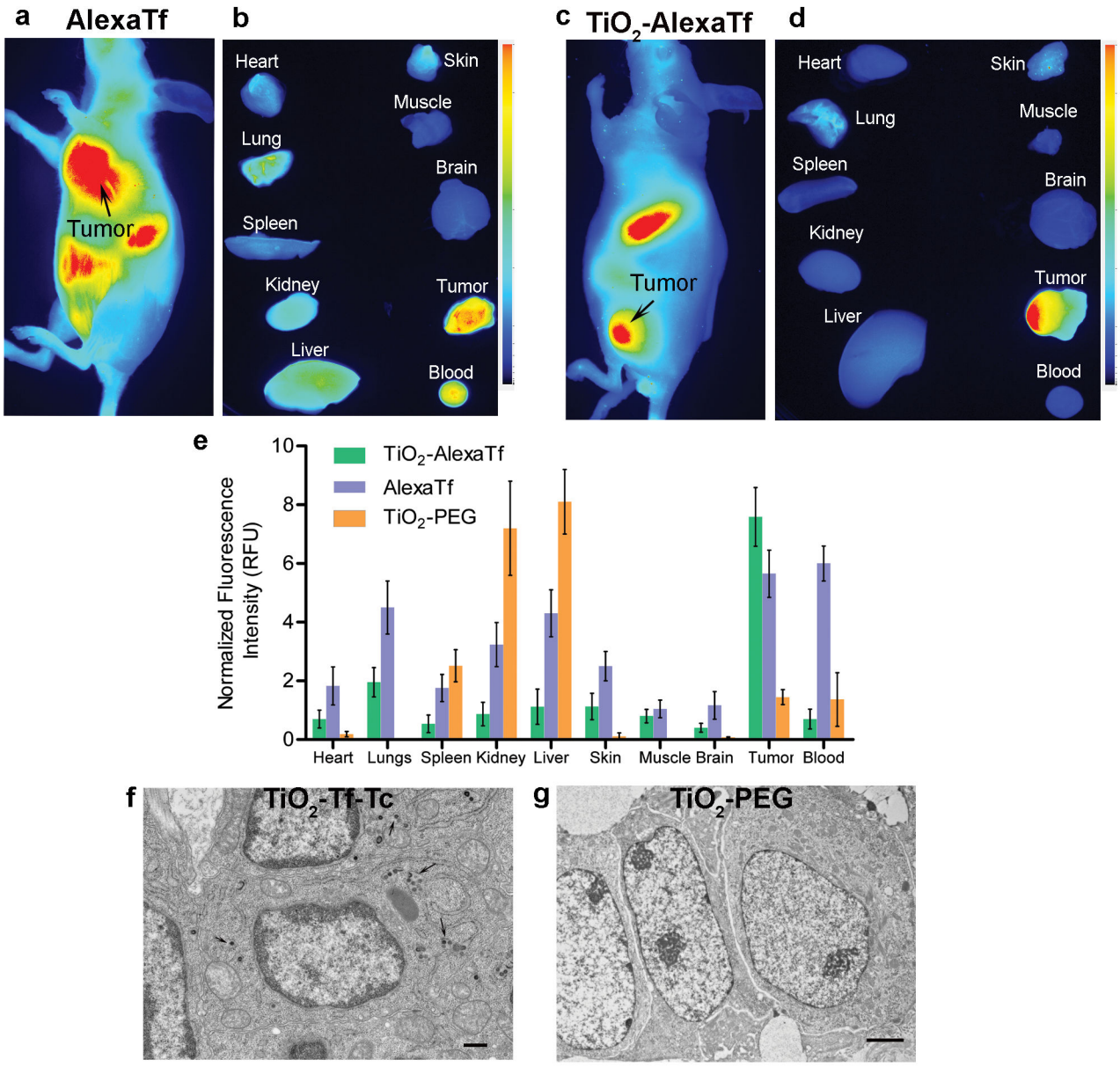

Figure 5. ***In vivo*** **biodistribution of NPS**

a, *In vivo* biodistribution profile of AlexaTf in HT1080 tumour bearing Athymic nude mice at 24 h following tail vein injection (n = 5). Experiments were replicated 3X. **b,** *Ex vivo* fluorescence image of dissected organs from (a). Notice the high fluorescence from blood suggesting circulating AlexaTf. **c,** *In vivo* biodistribution profile of TiO_2-AlexaTf in HT1080 tumour bearing Athymic nude mice at 24 h following tail vein injection (n = 5). **d,** *Ex vivo* fluorescence image of dissected organs from (c). Fluorescence imaging was performed using an excitation and emission wavelength of 685nm and 720 nm, respectively. **e,** *In vivo* biodistribution of TiO_2-AlexaTf AlexaTf and TiO_2-PEG alone in HT1080 tumour bearing Athymic nu/nu mice over 24 h. Intrinsic fluorescence of TiO_2 nanoparticles was used for the *ex vivo* imaging of TiO_2-PEG. Values are means ± s.e.m. (*n* = 5 mice per

group). **f,** TEM image of tumour sections showing localization of the TiO_2-Tf-Tc constructs (arrow) in tumour cells after i.v. administration. Scale bar, 500 nm **g,** TEM image of tumour sections of mice injected with TiO_2-PEG showing absence of TiO_2 in the tumour cells. Scale bar, 1μm. High tumour uptake and retention of Tf-coated NPS relative to non-tumour tissues demonstrate the feasibility of CRIT *via* i.v. administration of CR source following selective retention of the NPS in tumours.

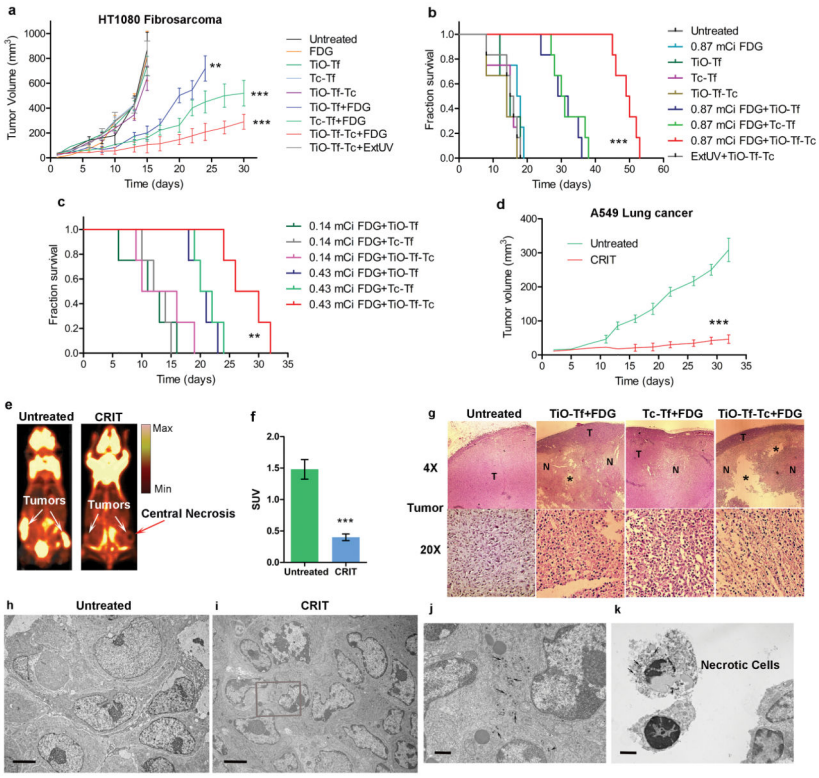

Figure 6. Evaluation of CRIT through systemically administered photoagents and FDG

a, *In vivo* CRIT through a one-time systemic administration of the constructs and FDG in HT1080 tumour bearing Athymic nu/nu mice. Values are means ± s.e.m. (n = 6 mice per group). $^{**}P < 0.01$, $^{***}P < 0.001$. Experiments were replicated 3X. **b,** Kaplan-Meier survival curves representing treatment with 0.87 mCi/0.1 ml FDG. *** $P < 0.001$. **c,** Survival curves representing treatment with 0.14 and 0. 43 mCi/0.1 ml FDG (n = 4 mice per group). Experiments were replicated 2X. $^{**}P < 0.01$. **d,** *In vivo* CRIT in A549 tumour bearing Athymic nu/nu mice using TiO_2-Tf-Tc and FDG. Values are means ± s.e.m. (n = 4 mice per group). Experiments were replicated 2X. $^{***}P < 0.001$. **e,** FDG-PET images of untreated (left) mouse (15 d) with bilateral HT1080 tumours and after CRIT (30 d), imaged by administering 0.19 mCi/0.1 ml FDG i.v. Notice the right tumour in mouse undergoing CRIT displays a necrotic zone. **f,** Standard uptake value of FDG is considerably low in mouse that underwent CRIT. $^{***}P < 0.001$. **g,** Histological analysis of H&E stained HT1080 tumour sections from an untreated mouse are compared to mice that underwent CRIT. Normal tumour tissue is marked as **T**, necrotic tissue as **N**, and denuded areas suggesting macrophage assisted clearance is marked as *. Magnified images show tumour-infiltrating lymphocytes in the treated tumour sections. **h,** TEM image of tumour section extracted from untreated mice showing healthy cells. Scale bar, 3 μm **i,** TEM image of tumour section extracted from mice that underwent CRIT showing majority of cells are apoptotic. Scale bar, 3 μm. **j,** Magnified TEM image of (i) showing internalized NPS (arrows) in apoptotic tumour cells. Scale bar, 500 nm. **k,** TEM image of tumour section from necrotic region showing necrotic cells with internalized NPS (arrows). Scale bar, 2 μm.

Disparate and regenerative cytotoxic free radicals from both Tc and TiO_2 in TiO_2 in TiO_2-Tf-Tc NPS utilized apoptosis and necrosis cell death pathways to enhance CRIT.

Table 1

Physico-chemical characterization of TiO_2-PEG, TiO_2-Tf and TiO_2-Tf-Tc constructs.

Sample	Hydrodynamic Diameter (nm)	Polydispersity Index	Zeta Potential (mV)	Mobility (μmcm/Vs)
TiO_2	454±40	1.00	−17.1±4.6	−1.34
TiO_2-PEG	268±26	0.23	4.28±1.9	0.33
TiO_2-Tf	106±18	0.08	− 7.77±3.7	− 0.61
TiO_2-Tf-Tc	108±13	0.09	− 7.36±3.6	− 0.57

The hydrodynamic size and zeta potential of the TiO_2 based constructs in phosphate buffered saline (PBS) were measured using a Malvern Zetasizer. Hydrodynamic diameter was extracted by cumulant analysis of the data and polydispersity index from cumulant fitting. Each value is the average of three experiments ± s.e.m. Experiments were replicated 3X.